36th AIAA Fluid Dynamics Conference and Exhibit, 5–8 June 2006, San Francisco CA

On Synchronization of Weighted Essentially Non-Oscillatory Methods

Ellen M. Taylor* and M. Pino Martín†
Princeton University, Princeton NJ 08544

Weighted essentially non-oscillatory (WENO) methods have been developed to simultaneously provide robust shock-capturing in compressible fluid flow and avoid excessive damping of fine-scale flow features such as turbulence. Under certain conditions in compressible turbulence, however, numerical dissipation remains unacceptably high even after optimization of the linear component that dominates in smooth regions. We demonstrate that a significant *non*linear source of dissipation error is due to a WENO implementation defect that we call the "synchronization deficiency," and we develop and evaluate a preliminary technique to mitigate its effects. Direct numerical simulations (DNS) include one-dimensional test cases and three-dimensional compressible isotropic turbulence. Although we find the current formulation of our mitigation technique to be quite successful for the one-dimensional problems, its efficacy is more modest in the turbulence simulations, and its cost-to-benefit ratio is uncomfortably high. We believe, however, that with further work it will be possible to alleviate these drawbacks.

I. Introduction

The detailed simulation of compressible turbulence requires numerical methods that simultaneously avoid excessive damping of spatial features over a large range of length scales and prevent spurious oscillations near shocks and shocklets (small transient shocks) through robust shock-capturing. Numerical schemes that were developed to satisfy these constraints include, among others, weighted essentially non-oscillatory (WENO) methods.[1] WENO schemes compute numerical fluxes using several different candidate stencils and form a final flux approximation by summing weighted contributions from each stencil. Smoothness measurements cause stencils that span large flow field gradients to be assigned small relative weights so that a nearly discontinuous shock would provide a weight of almost zero to any stencil containing it. In smooth regions, the relative values of the weights are designed to be optimal by some gauge such as maximum order of accuracy or maximum bandwidth-resolving efficiency.

Jiang and Shu[2] cast the WENO methodology into finite-difference form and provide an efficient implementation of robust and high-order-accurate WENO schemes. Unfortunately, these schemes often generate excessive numerical dissipation for detailed simulations of turbulence, especially for large-eddy simulations (LES).[3] WENO dissipation arises from two distinct sources: (i) the optimal stencil, which on its own describes a linear scheme, and (ii) the adaptation mechanism, which drives the final numerical stencil away from the optimal one. Bandwidth optimization can reduce the dissipation of the optimal stencil;[4,5] and Martín et al.[5] demonstrate that such a bandwidth-optimized WENO method indeed reduces numerical dissipation and provides accurate results for direct numerical simulations (DNS) of isotropic turbulence and turbulent boundary layers.

Nonetheless, engaging the nonlinear WENO adaptation mechanism still causes significant local dissipation that can negatively affect global flow properties. Though higher resolution compensates for this, in some cases adequately increasing the number of grid points is not feasible. There are two primary sources of nonlinear error: (i) the smoothness measurement that governs the application of WENO stencil adaptation

*Ph.D. Student and AIAA Member.
†Assistant Professor and AIAA Member.

and (ii) the coefficients of the individual candidate stencils that govern numerical accuracy when adaptation engages. Wang and Chen[6] have optimized both sources for upwind-biased WENO methods in linearized problems; Ponziani et al.[7] have optimized the second source for symmetric WENO methods in linear and nonlinear problems, including isotropic turbulence; and Henrick et al.[8] have optimized the first source for upwind-biased WENO methods in linear and nonlinear problems. Additionally, Taylor et al.[9,10] have optimized both sources for symmetric WENO methods in linear and nonlinear problems, including isotropic turbulence.

The purpose of this paper is to demonstrate that such approaches to reducing error contributions from nonlinear sources are hindered by an inextricable flaw in the current WENO methodology that we call the "synchronization deficiency." We furthermore develop and evaluate a preliminary technique to mitigate the effects of this deficiency for DNS of compressible turbulence. In Section II, we present relevant background material, including a description of the linearly-optimized symmetric WENO method that serves as our base method; Section III introduces the concept of the synchronization deficiency as well as numerical evidence of its consequences. Our procedure for partially repairing the deficiency is detailed in Section IV, and in Sections V and VI, we conduct numerical simulations of both one-dimensional inviscid problems and three-dimensional compressible isotropic turbulence to appraise the practical viability of this technique.

II. Background

A. WENO Methodology

We describe the symmetric WENO methodology[4,5] in the context of the one-dimensional advection equation,

$$\frac{\partial u}{\partial t} + \frac{\partial}{\partial x} f(u) = 0 \tag{1}$$

This model equation represents the decoupled forms of equations belonging to any system of hyperbolic conservation laws after a transformation from physical into characteristic space. If the spatial domain is discretized such that $x_i = i\Delta$, in which Δ is the grid spacing, and $u_i = u(x_i)$, Eq. (1) may be cast into the semidiscretized form

$$\frac{du_i}{dt} = -\frac{1}{\Delta}\left(\hat{f}_{i+\frac{1}{2}} - \hat{f}_{i-\frac{1}{2}}\right) \tag{2}$$

in which $\hat{f}_{i+1/2}$ is a numerical approximation of $f\big(u(x_{i+1/2})\big)$. Once the right-hand side of this expression has been evaluated, numerical techniques for solving ordinary differential equations, such as Runge-Kutta methods, may be employed to advance the solution in time. In order to ensure stability, procedures that approximate $f(u)$ split it into $f^+(u)$, which has a strictly non-negative derivative, and $f^-(u)$, which has a strictly non-positive one.

WENO schemes compute $\hat{f}^+_{i+1/2}$ through interpolating polynomials on a number of candidate stencils each containing r grid points. In the symmetric WENO method, there are $(r+1)$ stencils in total. The one fully upwinded stencil ranges from $(i-r+1)$ to i, the one fully downwinded stencil ranges from $(i+1)$ to $(i+r)$, and the other stencils fall in between these two extremes. Figure 1 provides a schematic of this arrangement for $r = 3$. Throughout this paper, we will abbreviate any WENO implementation in which the candidate stencils contain r points as "WENO-r."

If the flux approximation on stencil k, which contains r grid points, is designated q^r_k and the weight assigned to that stencil is ω_k, the final numerical approximation becomes

$$\hat{f}^+_{i+\frac{1}{2}} = \sum_{k=0}^{r} \omega_k q^r_k \tag{3}$$

Specifically, q^r_k emerge from polynomial interpolants of maximal order r and are defined as

$$q^r_k \Big|_{i+\frac{1}{2}} = \sum_{l=0}^{r-1} a^r_{kl}\, f(u_{i-r+k+l+1}) \tag{4}$$

in which a^r_{kl} are tabulated coefficients; and ω_k are normalized forms of weights Ω_k defined as

$$\Omega_k = \frac{C_k^r}{(\varepsilon + IS_k)^p} \tag{5}$$

in which ε prevents division by zero, IS_k is a smoothness measurement that becomes large when discontinuities are present within stencil k, and p may be varied to increase or decrease WENO adaptation sensitivity. $p = 1$ typically provides sufficient adaptation with minimal dissipation. In completely smooth regions, each stencil is equally desirable, and ω_k revert to the optimal weights C_k. As formulated by Jiang and Shu,[2]

$$IS_k = \sum_{m=1}^{r-1} \Delta^{2m-1} \int_{x_{i-1/2}}^{x_{i+1/2}} \left[\frac{\partial^m}{\partial x^m} q_k^r(x) \right]^2 dx \tag{6}$$

in which $q_k^r(x)$ is an interpolating polynomial for the flux that may or may not be the same as the one that leads to $q_k^r\big|_{i+1/2}$ in Eq. (4). Equivalently,

$$IS_k = \sum_{l=0}^{r-1} \sum_{m=0}^{r-1} d_{klm}^r \, f(u_{i-r+k+l+1}) \, f(u_{i-r+k+m+1}) \tag{7}$$

in which d_{klm}^r are the coefficients that arise from Eq. (6).

The corresponding stencil diagram for $\hat{f}_{i+1/2}^-$ is simply a mirror image of Fig. 1. Because the total number of data points available to the symmetric WENO algorithm is $2r$, its maximum order of accuracy is also $2r$; however, the particular implementations employed in the current work have bandwidth-optimized optimal stencils that prevent more than rth-order accuracy.[4,5] In practice, the weight of the fully downwinded stencil ω_r is artificially constrained to be no greater than the least of the others so that adverse stability effects are avoided.

The continuity of the WENO weighting process allows the performance characteristics of the final numerical stencil to theoretically fall anywhere between those of the least favorable candidate stencil and those of the optimal stencil. In order to gauge this variation quantitatively but efficiently in a flow field, Weirs[4] proposed a combination of the adaptive stencil weights called the nonlinearity index (NI). It is essentially a measure of the degree of departure from the optimal stencil and is defined as

$$NI = \left(\sum_{k=0}^{r} \left[1 - \frac{(r+1)\,(\Omega_k / C_k)}{\sum_{l=0}^{r} (\Omega_l / C_l)} \right]^2 \right)^{\frac{1}{2}} \tag{8}$$

This definition forces NI to always be non-negative, and only the optimal stencil can provide a value of zero. It reaches its theoretical maximum, which is r, when any one candidate stencil is chosen exclusively. We will often report NI in terms of its normalized value $NI' = NI/r$.

B. Relative Smoothness Limiter

Building on a suggestion by Jiang and Shu,[2] Taylor et al.[9,10] have devised a modification of the standard WENO smoothness measurement in Eq. (6) known as the relative smoothness limiter. This technique forcibly imposes the WENO optimal stencil wherever the ratio of maximum to minimum smoothness measurement (among the collection of candidate stencils) is less than a threshold A_{RL}. IS_k is first computed normally; then

$$IS_k = \begin{cases} 0, & R(IS) < A_{RL} \\ IS_k, & \text{otherwise} \end{cases} \tag{9}$$

in which

$$R(IS) = \frac{\max\limits_{0 \le k \le r} IS_k}{\varepsilon + \min\limits_{0 \le k \le r} IS_k} \tag{10}$$

and in turn ε is the value employed in Eq. (5). Because the threshold A_{RL} applies to a ratio of smoothness measurements rather than their raw dimensional values, it is broadly effective without adjustment for a wide variety of flow field configurations. Taylor et al.[9,10] set $A_{RL} = 10$, and any WENO method that employs the relative limiting procedure with this value will be referred to in this paper as WENO-RL.

III. Synchronization Deficiency

A. Theory

In theory, the performance characteristics (e.g. bandwidth-resolving capabilities) of the least favorable WENO candidate stencil dictate a definitive lower bound on the performance characteristics of any possible final numerical stencil. In practice, however, this is not true.

Consider Eq. (2), the left-hand side of which depends on a fixed combination of $\hat{f}_{i+1/2}$ and $\hat{f}_{i-1/2}$. According to Eqs. (3) and (4),

$$\hat{f}_{i+\frac{1}{2}} = \sum_{k=0}^{r} \omega_k \sum_{l=0}^{r-1} a_{kl}^r \, f_{i-r+k+l+1} \tag{11a}$$

$$\hat{f}_{i-\frac{1}{2}} = \sum_{k=0}^{r} \omega_k \sum_{l=0}^{r-1} a_{kl}^r \, f_{i-r+k+l} \tag{11b}$$

and so

$$\begin{aligned} \frac{du_i}{dt} &= -\frac{1}{\Delta}\left(\hat{f}_{i+\frac{1}{2}} - \hat{f}_{i-\frac{1}{2}}\right) \\ &= -\frac{1}{\Delta}\sum_{k=0}^{r} \omega_k \left[a_{k,r-1}^r \, f_{i+k} - a_{k,0}^r \, f_{i-r+k} + \sum_{l=1}^{r-1} \left(a_{k,l-1}^r - a_{kl}^r\right) f_{i-r+k+l} \right] \\ &= -\frac{1}{\Delta}\sum_{k=0}^{r} \omega_k \sum_{l=0}^{r} b_{kl}^r \, f_{i-r+k+l} \end{aligned} \tag{12}$$

in which coefficients can be equated to yield

$$b_{kl}^r = \begin{cases} -a_{k,0}^r, & l = 0 \\ a_{k,l-1}^r - a_{kl}^r, & 0 < l < r \\ a_{k,r-1}^r, & l = r \end{cases} \tag{13}$$

The coefficients b_{kl}^r, *not* a_{kl}^r, are the relevant parameters for determining and optimizing the properties of the kth candidate stencil. Since b_{kl}^r are independent of the adaptive quantities ω_k, the performance characteristics of individual candidates appear to be guaranteed regardless of local WENO adaptation. The flaw in this argument is the implicit assumption in Eq. (11) that ω_k are equal for $\hat{f}_{i+1/2}$ and $\hat{f}_{i-1/2}$.

The smoothness measurement IS_k, as presented in Eq. (7), depends entirely on the flux information available within stencil k, which spans slightly different points for $\hat{f}_{i+1/2}$ and $\hat{f}_{i-1/2}$. Because the collections of data values on the two versions of the stencil may be unequal, the associated stencil weights ω_k must be assumed to vary. If we designate $\omega_k^{\pm}$ to mean the ω_k that belong to $\hat{f}_{i\pm1/2}$, Eq. (11) becomes

$$\hat{f}_{i+\frac{1}{2}} = \sum_{k=0}^{r} \omega_k^{+} \sum_{l=0}^{r-1} a_{kl}^r \, f_{i-r+k+l+1} \tag{14a}$$

$$\hat{f}_{i-\frac{1}{2}} = \sum_{k=0}^{r} \omega_k^{-} \sum_{l=0}^{r-1} a_{kl}^r \, f_{i-r+k+l} \tag{14b}$$

and in turn Eq. (12) becomes

$$\begin{aligned} \frac{du_i}{dt} &= -\frac{1}{\Delta}\left(\hat{f}_{i+\frac{1}{2}} - \hat{f}_{i-\frac{1}{2}}\right) \\ &= -\frac{1}{\Delta}\sum_{k=0}^{r} \omega_k^{+} \left[a_{k,r-1}^r \, f_{i+k} - \frac{\omega_k^{-}}{\omega_k^{+}} a_{k,0}^r \, f_{i-r+k} + \sum_{l=1}^{r-1} \left(a_{k,l-1}^r - \frac{\omega_k^{-}}{\omega_k^{+}} a_{kl}^r\right) f_{i-r+k+l} \right] \\ &= -\frac{1}{\Delta}\sum_{k=0}^{r} \omega_k^{+} \sum_{l=0}^{r} \widetilde{b_{kl}^r} \, f_{i-r+k+l} \end{aligned} \tag{15}$$

in which coefficients can be equated to yield

$$\widetilde{b^r_{kl}} = \begin{cases} -\frac{\omega_k^-}{\omega_k^+} a^r_{k,0}, & l = 0 \\ a^r_{k,l-1} - \frac{\omega_k^-}{\omega_k^+} a^r_{kl}, & 0 < l < r \\ a^r_{k,r-1}, & l = r \end{cases} \tag{16}$$

The relevant parameters for determining and optimizing the properties of the kth candidate stencil are now the new coefficients $\widetilde{b^r_{kl}}$. These, unlike the old b^r_{kl}, do depend on the adaptive quantities $\omega_k^{\pm}$; and, since a^r_{kl} are fixed, $\widetilde{b^r_{kl}} = b^r_{kl}$ if and only if $\omega_k^- = \omega_k^+$. Note that equality necessarily holds when $\hat{f}_{i\pm1/2}$ both employ the optimal stencil weights C^r_k, so this synchronization deficiency is irrelevant in completely smooth flow regions. In regions in which WENO adaptation has engaged, however, $\widetilde{b^r_{kl}} \neq b^r_{kl}$ can force the actual individual stencil characteristics to diverge from the expected theoretical properties described by b^r_{kl}.

B. Numerical Evidence

Though the WENO synchronization deficiency is certainly valid from a mathematical standpoint, variation between b^r_{kl} and $\widetilde{b^r_{kl}}$ may in practice be negligibly small. After all, the candidate stencils for $\hat{f}_{i-1/2}$ are displaced from those of $\hat{f}_{i+1/2}$ by only one point. We investigate this possibility by implementing a naive forcibly synchronized WENO (SWENO) method for the one-dimensional advection equation of Eq. (1). After obtaining the normalized stencil weights ω_k according to Section II.A, we set

$$\langle \Omega_k \rangle = \frac{1}{2} \left(\omega_k^+ + \omega_k^- \right) \tag{17}$$

and then normalize $\langle \Omega_k \rangle$ to form the synchronized stencil weights $\langle \omega_k \rangle$ that apply to both $\hat{f}_{i+1/2}$ and $\hat{f}_{i-1/2}$.

The effects of synchronizing a bandwidth-optimized WENO-4 scheme in this manner are presented in Fig. 2, which depicts a linearly advected sine wave with seven points per wavelength after twenty wavelength-times. For reference we include results from the original (unsynchronized) WENO-4 scheme, both with and without stencil adaptation permitted. Figure 2(a) shows that, while the WENO-4 scheme causes notable dissipation, the SWENO-4 scheme maintains the proper wave shape nearly as faithfully as when adaptation is prohibited. In Fig. 2(b), we plot the nonlinearity index NI' for each of these schemes to demonstrate that the improvement offered by the SWENO method is not due simply to closer conformance to the optimal stencil. The decrease in overall NI' from the adaptation-permitted WENO-4 scheme to the adaptation-prohibited WENO-4 scheme dwarfs the decrease from the former to the SWENO-4 scheme, yet the SWENO-4 flow solution is almost equivalent to the adaptation-prohibited WENO-4 solution.

This exercise proves that the synchronization deficiency is not merely a mathematical curiosity; its consequences unquestionably contaminate the results of numerical simulations.

IV. Forced Synchronization

Attempting to extend the forcibly synchronized WENO method of Section III.B to non-smooth initial data explains our previous warning that this approach is naive. Consider a linearly advected perfect shock located somewhere between points x_{i-1} and x_i as sketched for $r = 3$ in Fig. 3. Without explicitly calculating the smoothness measurements IS_k and resulting weights ω_k, we can still qualitatively determine that a candidate stencil receives small weight if it crosses the discontinuity and large weight otherwise. (Recall that the fully downwinded stencil is never allowed to hold more weight than the least-weighted of the others.) According to this principle, the bold stencils in the second half of Fig. 3 are those favored independently for calculating $\hat{f}_{i\pm1/2}$, and they are clearly mutually exclusive. If ω_k are to be synchronized, some form of compromise is necessary; it is this compromise that undermines the WENO shock-capturing capability.

Before proceeding into the supporting argument, we first modify Eq. (17) so that it contains a free parameter α:

$$\langle \Omega_k \rangle = \alpha \left(M_+ - M_- \right) + M_- \tag{18}$$

in which

$$M_- = \min\left(\omega_k^+, \omega_k^-\right)$$
$$M_+ = \max\left(\omega_k^+, \omega_k^-\right) \tag{19}$$

$\alpha = 0$ is equivalent to $\langle\Omega_k\rangle = \min\left(\omega_k^+, \omega_k^-\right)$; $\alpha = \frac{1}{2}$ is equivalent to Eq. (17); and $\alpha = 1$ is equivalent to $\langle\Omega_k\rangle = \max\left(\omega_k^+, \omega_k^-\right)$. Using these three representative values to forcibly synchronize the stencil weights of the ideal configuration described in Fig. 3, we arrive at the results in Tables 1-3. A circle ($\circ$) indicates favor, a cross ($\times$) indicates disfavor, and a dash ($-$) indicates no favor either way. For $\alpha = 0$, all candidate stencils are equally disfavored, and without one or several distinctly superior candidates, the WENO method reverts to its optimal stencil, which is appropriate only for smooth regions. For $\alpha = \frac{1}{2}$ and $\alpha = 1$, the 1st and 3rd synchronized stencil weights are clearly negligible compared to the other two, but the discontinuity-spanning stencils ($k = 2$ for $\hat{f}_{i+1/2}$ and $k = 0$ for $\hat{f}_{i-1/2}$) fall within the latter, not the former. Thus none of these cases adequately captures shocks.

In order to preserve the robust shock-capturing capability of unsynchronized WENO methods, we must selectively suspend synchronization in neighborhoods of strong discontinuities. The form of our criterion for this switch arises naturally from the root cause of the perfect-shock failure above, which is the mutual exclusivity of the candidate stencils favored for computing $\hat{f}_{i\pm1/2}$. In mathematical terms, for the scenario depicted in Fig. 3, the ratio of $\min\left(\omega_k^+, \omega_k^-\right)$ to $\max\left(\omega_k^+, \omega_k^-\right)$ is much less than unity for *all* values of k for which ω_k^+ and ω_k^- are not both negligible. We prefer, however, the more conservative condition that this ratio be much less than unity for *at least one* value of k, regardless of the magnitudes of $\omega_k^\pm$, because it promotes greater stability and also requires only one variable parameter. We designate the individual suspension indicators ψ_k as

$$\psi_k = \begin{cases} 1, & \frac{\varepsilon + M_-}{\varepsilon + M_+} \leq \beta \\ 0, & \text{otherwise} \end{cases} \tag{20}$$

in which ε is the value employed in Eq. (5) and β is a free parameter; and from these we define the master suspension indicator Ψ as

$$\Psi = \begin{cases} 1, & \sum_{k=0}^{r} \psi_k > 0 \\ 0, & \text{otherwise} \end{cases} \tag{21}$$

If $\Psi = 0$ ("false"), synchronization is allowed to proceed according to Eq. (18); if $\Psi = 1$ ("true"), synchronization is suspended, leaving the original stencil weights $\omega_k^\pm$ in place.

The addition of conditional suspension of synchronization to the forcibly synchronized WENO (SWENO) method grants it full viability as a numerical method and completes the theoretical framework of this section. What remains are two practical considerations. First, an SWENO scheme with r points per candidate stencil requires significantly more computational time than an unsynchronized WENO scheme with the same number of points. Efficient WENO implementations recognize that $\hat{f}_{i+1/2}$ at grid point $i = j$ is equivalent to $\hat{f}_{i-1/2}$ at point $(i = j + 1)$ and therefore calculate only $\hat{f}_{i+1/2}$ at each point. Synchronization, however, introduces the possibility that $\hat{f}_{i+1/2}$ at $i = j$ may depend on different stencil weights than those producing $\hat{f}_{i-1/2}$ at $i = j+1$; thus SWENO methods must calculate *both* $\hat{f}_{i\pm1/2}$ at every grid point. Also of practical concern are appropriate values for the variable parameters α and β. β's qualitative role is clear: it must be large enough to suspend synchronization wherever stability demands so and small enough to permit synchronization elsewhere. The role of α is less clear, even from a qualitative standpoint, due to the re-normalization that transforms the synchronized weights $\langle\Omega_k\rangle$ into $\langle\omega_k\rangle$.

Figure 4 provides a rough constraint on plausible values for β by plotting the weight ratio M_-/M_+ on each WENO candidate stencil for an instantaneous sinusoidal signal with six points per wavelength. A WENO-3 scheme is addressed in Fig. 4(a) and a WENO-4 scheme in Fig. 4(b). Although the analytic signal is smooth, the low numerical resolution is approaching the point at which these variations become indistinguishable from discontinuities; therefore WENO adaptation is already strongly engaged, as indicated by the displayed weight ratios. The range of ratios attained over all stencils is similar for the WENO-3 and WENO-4 schemes, and restricting β to fall below 0.1 would be conservatively sufficient to avoid unnecessary suspension of synchronization in either case. Presumably, this bound would also be sufficient for any other perfectly sinusoidal signal of higher resolution.

V. One-Dimensional Euler Simulations

A. Shock Tube

The inviscid shock tube problem probes the ability of a shock-capturing method to capture isolated fluid flow discontinuities (both shocks and contact discontinuities) in an environment as free as possible from other complicating factors. Our simulations set conditions at the right boundary to be atmospheric with zero velocity and conditions at the left boundary to be the same except for a doubling of the density and pressure. Initially, a discontinuous jump exists between the two states at $x/L = 0.5$, in which L is the length of the tube; and we evolve the simulations in time until $t = 0.3\,L/a$, in which a is the initial speed of sound. For orientation purposes, Fig. 5 displays density profiles computed by unsynchronized bandwidth-optimized WENO-3 and WENO-4 schemes on 129 grid points versus a converged profile computed by the WENO-4 scheme on an excessively fine grid of 2049 points. From left to right, the flow features are the leftward-moving rarefaction wave, the rightward-moving contact discontinuity, and the rightward-moving shock.

Figure 6 presents the results of forcibly synchronizing the low-resolution WENO-3 scheme using various values for the parameters α and β. Because the data near the rarefaction wave and contact discontinuity are consistent between each of the methods, this figure focuses on the shock; the density profiles of Fig. 6(a) show that its location varies moderately. For fixed β, increasing α pushes the shock to the right, and increasing β slightly narrows the range of this variation. The best match to the original WENO-3 scheme is provided by $(\beta = 0.05, \alpha = 0.5)$ although $(\beta = 0.01, \alpha = 0.5)$ also produces acceptable results. In Fig. 6(b), we more closely examine the SWENO suspension mechanism by plotting a version of the master synchronization suspension indicator Ψ over a sketch of the WENO-3 density profile. Since the Euler equations generate both positive- and negative-traveling fluxes $f^+(u)$ and $f^-(u)$, we adopt the convention here that $\Psi = 1$ implies $\Psi = 1$ for both, $\Psi = \frac{1}{2}$ implies $\Psi = 1$ for one but not the other, and $\Psi = 0$ implies $\Psi = 1$ for neither. Overall, a generous region of double-suspension encases the shock, but for most parameter combinations, especially those with $\beta = 0.01$, the individual suspension profiles bounce erratically between double-, single-, and even no suspension. Only $(\beta = 0.05, \alpha = 0.5)$ avoids this bouncing.

The results of synchronizing the low-resolution WENO-4 scheme are presented in Fig. 7. Like the SWENO-3 data, the density profiles of Fig. 7(a) reveal that, for $\beta = 0.01$, the location of the shock shifts to the right as α increases. Unlike the SWENO-3 data, such a variation is entirely absent when $\beta = 0.05$, and all values of α lead to a shock propagation speed that precisely matches that of the original WENO-4 scheme. In Fig. 7(b), the master suspension indicator Ψ echoes these similarities and differences. As before, for $\beta = 0.01$, the individual suspension profiles within and around the shock bounce unpredictably between double- and single-suspension though none now drop to zero. Now, however, all SWENO schemes with $\beta = 0.05$ maintain strict double-suspension across the shock and transition sharply on either side to no suspension.

B. Shu-Osher Problem

The Shu-Osher problem places smooth density fluctuations upstream of a moving shock front to probe the ability of a shock-capturing method to capture discontinuities embedded within pseudoturbulence without damaging the fine structures. Our simulations set conditions at the right boundary to be atmospheric with zero velocity and conditions at the left boundary such that the shock between the two states experiences a relative incoming Mach number of three. Sinusoidal density fluctuations are imposed upstream of this shock with wavelength $\lambda = \frac{1}{8}L$ and excursions of $\pm 0.2\rho_R$, in which the subscript R indicates the right boundary. Initially, the shock is positioned at $x/L = \lambda$, and we evolve the simulations in time until $t = 0.2\,L/a_R$. For orientation purposes, Fig. 8 displays density profiles computed by unsynchronized bandwidth-optimized WENO-3 and WENO-4 schemes on 193 grid points versus a converged profile computed by the WENO-4 scheme on an excessively fine grid of 2049 points. An undisturbed portion of the original fluctuation field lies upstream of the main shock, immediately downstream is a region of physically correct high-frequency fluctuations, and further downstream is a region of low-frequency fluctuations with interspersed shocklets.

Figure 9 presents the results of forcibly synchronizing the low-resolution WENO-3 scheme using the same values for the parameters α and β as in the shock tube simulations. Omitted from the density profiles of Fig. 9(a) are two of the SWENO cases with $\beta = 0.01$ because these all diverge substantially from both the converged and under-resolved WENO-3 profiles and one sample is sufficient for illustration. In fluctuation regions that have already passed through the main shock, setting $\beta = 0.01$ leads to baseline densities that

are significantly higher than their proper values, especially among the high-frequency fluctuations. Also, the predicted position of the main shock noticeably leads its correct position. Setting $\beta = 0.05$, on the other hand, produces none of these deficiencies, and, additionally, these SWENO schemes meaningfully reduce dissipation in the high-frequency region compared to the original WENO-3 scheme. Note that the small phase error highlighted by this improvement was already present in the WENO-3 results. In Fig. 9(b), we plot the master suspension indicator Ψ for these accurate SWENO cases only. Although the competition between single-suspension and no suspension is too complex to summarize generally, double-suspension always occurs near the shocklets and main shock and never anywhere else.

The results of synchronizing the low-resolution WENO-4 scheme are presented in Fig. 10. We include only one of the SWENO cases with $\beta = 0.01$ among the density profiles of Fig. 10(a) because all three exhibit subtle indications of instability in the high-frequency region and slightly overpredict the position of the main shock. As before, setting $\beta = 0.05$ eliminates these deviations and meaningfully reduces dissipation in the high-frequency region, most noticeably near its junction with the post-interaction low-frequency region to the left. The three profiles of the master suspension indicator Ψ that we plot in Fig. 10(b) again indicate consistent double-suspension close to the shocklets and main shock and nowhere else, but these double-suspension regions are now wider, as are many areas of no suspension.

VI. Three-Dimensional Isotropic Turbulence Simulations

Decaying three-dimensional isotropic turbulence is a canonical flow field that realistically represents the small scales of many turbulent flows and, if compressible, can generate shocklets that are strong and numerous enough to require shock-capturing methods. Its physical domain is a three-dimensional cube with periodic boundary conditions and an edge length that encompasses a sufficient sample of large-scale turbulence structures; an evenly-spaced Cartesian grid discretizes this domain into N^3 points. We conduct direct numerical simulations (DNS) of isotropic turbulence that approximate the convective terms of the Navier-Stokes equations with various WENO and SWENO methods, the viscous terms with fourth-order-accurate finite differences, and time advancement with a third-order-accurate low-storage Runge-Kutta scheme.

The following two nondimensional parameters are important for characterizing the state of isotropic turbulence: the Reynolds number based on the Taylor microscale

$$Re_\lambda = \frac{\langle\rho\rangle\, u'_{\text{rms}}\lambda}{\langle\mu\rangle} \tag{22}$$

in which u'_{rms} is the root-mean-squared velocity (per component) and λ is the Taylor microscale, and the turbulent Mach number

$$M_t = \frac{q}{\langle a\rangle} \tag{23}$$

in which $\langle a\rangle$ is the average speed of sound and q is the root-mean-squared total velocity magnitude. Note that Re_λ and M_t are not constant throughout a simulation because the global strength of the turbulent fluctuations steadily decays over time without external forcing, which we do not include. The combinations of Re_λ and M_t with which we initialize our flow fields are listed in Table 4 along with the resolution required for a converged WENO-RL-4 solution (N_+^3) and a lower resolution (N_-^3) that we use to test the SWENO methods. Each initial field is a solenoidal approximation that we evolve on 256^3 grid points for the duration of the initialization transient, which we find to be roughly $1.5\,\tau_t$, where τ_t is the initial state's reference time λ/u'_{rms}. We then filter the resulting field to an appropriate grid resolution from Table 4 and begin our data runs.

Figure 11 presents results pertaining to one sample set of turbulence conditions (initial $Re_\lambda = 50$ and $M_t = 0.7$) using the original WENO-3 scheme, various SWENO-3 schemes, and, for comparison, the relative-limited WENO-3 (WENO-RL-3) scheme.[9,10] Because $\beta = 0.05$ has proven to be consistently more robust than $\beta = 0.01$ in one-dimensional test cases, we restrict our attention in this section to the former. In Fig. 11(a), we track the temporal evolution of average turbulent kinetic energy $\langle\rho q^2\rangle$ normalized by its value at $t/\tau_t = 1.5$ (when the test runs begin). The converged solution indicates the rate of energy decay that is natural, and the remaining solutions, on coarser grids, exhibit varying degrees of additional dissipation due to their numerical methods. The SWENO schemes succeed in reducing excess dissipation by a small amount; however, this improvement falls far short of the reduction achieved by the WENO-RL scheme. Information

of a more local nature is available through the instantaneous energy spectra of Fig. 11(b), which displays nondimensional spectra for each of the schemes at $t/\tau_t = 3.0$. Note that the offset between the converged solution and the others at low wavenumbers is merely an artifact of the normalization. Within the zoomed area, the WENO-RL solution tracks slightly more closely to the converged solution than the other coarse-grid cases; otherwise, there are no discernible differences.

A similar presentation of results for WENO-4 and SWENO-4 schemes under the same turbulence conditions is provided by Fig. 12. Figure 12(a) tracks the temporal evolution of average turbulent kinetic energy, and, aside from a systematic decrease in global dissipation due to the greater number of stencil points, we observe trends mostly in line with those of Fig. 11(a). The only difference is that a strong variation with the synchronization parameter α is now apparent. Unlike the SWENO-3 results, however, the coarse-grid energy spectra of Fig. 12(b) reveal no measurable differences between any of the WENO-4 or SWENO-4 solutions, including the WENO-RL solution.

We adopt as a convenient measure of global numerical dissipation the time-integrated decay of average turbulent kinetic energy beyond that which occurs naturally in converged solutions. In Fig. 13, we display graphical comparisons of this quantity for WENO-3 and SWENO-3 schemes under all isotropic turbulence conditions listed in Table 4 and for all tested synchronization parameters. Errors are normalized so that the error of the original WENO-3 scheme is always unity. In general, particular choices of turbulence conditions do not drastically influence any of the results, and the WENO-RL scheme consistently outperforms each of the SWENO schemes. As α increases, SWENO dissipation error consistently decreases, and sensitivity to α increases moderately with both Re_λ and M_t (independently). As M_t increases, the efficacy of the relative limiter slowly diminishes so that the performance gap between the WENO-RL and SWENO schemes narrows slightly. In Fig. 14, we display our numerical dissipation measure similarly for the WENO-4 and SWENO-4 schemes, and most of the previously observed trends hold for these as well. Now, however, performance is considerably more sensitive to precise values of α; and setting $\alpha = 0.1$ appears to increasingly destabilize simulations for higher Re_λ and lower M_t.

VII. Conclusions

The WENO synchronization deficiency unquestionably generates excessive numerical dissipation when stencil adaptation engages and thus hinders the ability of WENO methods to accurately resolve fine scales of compressible turbulence. Because forced synchronization roughly doubles the computational requirements of an already expensive methodology, care must be taken to ensure that the cure is not worse than the affliction; however, the consequences of the synchronization deficiency are serious enough that potential improvements in grid-convergence rates can outweigh the additional fixed-grid expense.

Selectively-suspended forced synchronization, as currently formulated, can be highly successful in one-dimensional test cases for certain combinations of the synchronization parameters α and β. Although the following trend is not without deviations, setting $\beta = 0.05$ generally allows SWENO schemes to faithfully predict the location of the shock front in the shock tube problem and also to avoid instabilities within the Shu-Osher problem's shock-pseudoturbulence interaction. Furthermore, subject to this constraint, both the SWENO-3 and SWENO-4 methods significantly reduce dissipation in the high-frequency region of the Shu-Osher problem even though synchronization is only partially engaged throughout much of it.

The forced-synchronization technique is less successful, but still useful, in simulations of three-dimensional compressible isotropic turbulence. SWENO schemes reduce global dissipation by only about one-third to one-half of the amount achieved by the previously developed modification known as the relative smoothness limiter, which requires virtually no additional computational expense. Interestingly, while the energy spectrum of the WENO-RL-3 scheme is marginally closer to the converged spectrum within the inertial range than the original WENO-3 spectrum, none of the SWENO-3 spectra deviates noticeably from the original. Because the various WENO-4 methods produce no such variation, the significance of this observation is unclear and may be none at all. The dissipation reduction of the SWENO method appears to improve with increasing α, but we caution against drawing too firm a conclusion from this. On the one hand, moderate instabilities may be mimicking an additional decrease in dissipation in the global view, and on the other hand, unstable excursions should trigger increased WENO adaptation and hence counter-dissipation. More localized inspections of the flow fields are necessary to resolve this ambiguity.

We will continue our investigation into the WENO synchronization deficiency and techniques to mitigate its effects. One line of questioning is the possibility of a smooth rather than abrupt transition between

forced synchronization and the suspension thereof; another is the possibility of a supplementary condition, mirroring Eq. (20), for forcibly imposing the WENO optimal stencil in nearly smooth regions. A forced synchronization procedure that is both robust and broadly effective for a variety of flow configurations will be worth its computational expense.

Acknowledgments

This work was sponsored by the National Science Foundation under Grant CTS-0238390. Computational resources were provided by the CRoCCo Laboratory at Princeton University.

References

[1]Liu, X.-D., Osher, S., and Chan, T., "Weighted Essentially Non-Oscillatory Schemes," *Journal of Computational Physics*, Vol. 115, No. 1, 1994, pp. 200–12.

[2]Jiang, G.-S. and Shu, C.-W., "Efficient Implementation of Weighted ENO Schemes," *Journal of Computational Physics*, Vol. 126, No. 1, 1996, pp. 202–28.

[3]Garnier, E., Mossi, M., Sagaut, P., Comte, P., and Deville, M., "On the Use of Shock-Capturing Schemes for Large-Eddy Simulations," *Journal of Computational Physics*, Vol. 153, No. 1, 1999, pp. 273–311.

[4]Weirs, V. G., *A Numerical Method for the Direct Simulation of Compressible Turbulence*, Ph.D. thesis, University of Minnesota, December 1998.

[5]Martín, M. P., Taylor, E. M., Wu, M., and Weirs, V. G., "A Bandwidth-Optimized WENO Scheme for the Direct Numerical Simulation of Compressible Turbulence," Journal of Computational Physics in press.

[6]Wang, Z. J. and Chen, R. F., "Optimized Weighted Essentially Nonoscillatory Schemes for Linear Waves with Discontinuity," *Journal of Computational Physics*, Vol. 174, No. 1, 2001, pp. 381–404.

[7]Ponziani, D., Pirozzoli, S., and Grasso, F., "Development of Optimized Weighted-ENO Schemes for Multiscale Compressible Flows," *International Journal for Numerical Methods in Fluids*, Vol. 42, No. 9, 2003, pp. 953–77.

[8]Henrick, A. K., Aslam, T. D., and Powers, J. M., "Mapped Weighted Essentially Non-Oscillatory Schemes: Achieving Optimal Order Near Critical Points," *Journal of Computational Physics*, Vol. 207, No. 2, 2005, pp. 542–67.

[9]Taylor, E. M., Wu, M., and Martín, M. P., "Optimization of Nonlinear Error Sources for Weighted Essentially Non-Oscillatory Methods in Direct Numerical Simulations of Compressible Turbulence," Paper 2006–1091, American Institute of Aeronautics and Astronautics, 2006.

[10]Taylor, E. M., Wu, M., and Martín, M. P., "Optimization of Nonlinear Error for Weighted Essentially Non-Oscillatory Methods in Direct Numerical Simulations of Compressible Turbulence," Submitted to Journal of Computational Physics.

$\alpha = 0$

k	ω_k^+	ω_k^-	$\langle\Omega_k\rangle$
0	×	○	×
1	×	×	×
2	○	×	×
3	×	×	×

Table 1. WENO-3 candidate stencil weights for the perfect shock of Fig. 3 before and after naively forced synchronization that sets $\langle\Omega_k\rangle = \min(\omega_k^+, \omega_k^-)$. (○): favored, (×): disfavored, (–): neither.

$\alpha = \frac{1}{2}$

k	ω_k^+	ω_k^-	$\langle\Omega_k\rangle$
0	×	○	–
1	×	×	×
2	○	×	–
3	×	×	×

Table 2. WENO-3 candidate stencil weights for the perfect shock of Fig. 3 before and after naively forced synchronization that sets $\langle\Omega_k\rangle = \frac{1}{2}(\omega_k^+ + \omega_k^-)$. (○): favored, (×): disfavored, (–): neither.

$\alpha = 1$

k	ω_k^+	ω_k^-	$\langle\Omega_k\rangle$
0	×	○	○
1	×	×	×
2	○	×	○
3	×	×	×

Table 3. WENO-3 candidate stencil weights for the perfect shock of Fig. 3 before and after naively forced synchronization that sets $\langle\Omega_k\rangle = \max(\omega_k^+, \omega_k^-)$. (○): favored, (×): disfavored, (–): neither.

Re_λ	M_t	N_+^3	N_-^3
35	0.4 0.7 1.0	128^3	64^3
50	0.4 0.7 1.0	160^3	96^3
75	0.4 0.7 1.0	192^3	128^3

Table 4. Governing parameter initial values and grid resolutions for direct numerical simulations of compressible isotropic turbulence. N_+^3 grids produce converged reference solutions, and N_-^3 grids are for active testing.

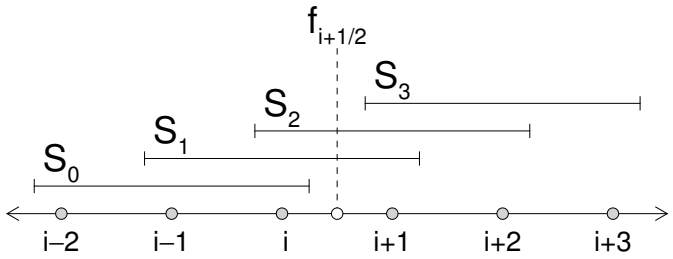

Figure 1. Symmetric WENO-3 candidate stencils for approximating the numerical flux $\hat{f}_{i+1/2}^+$.

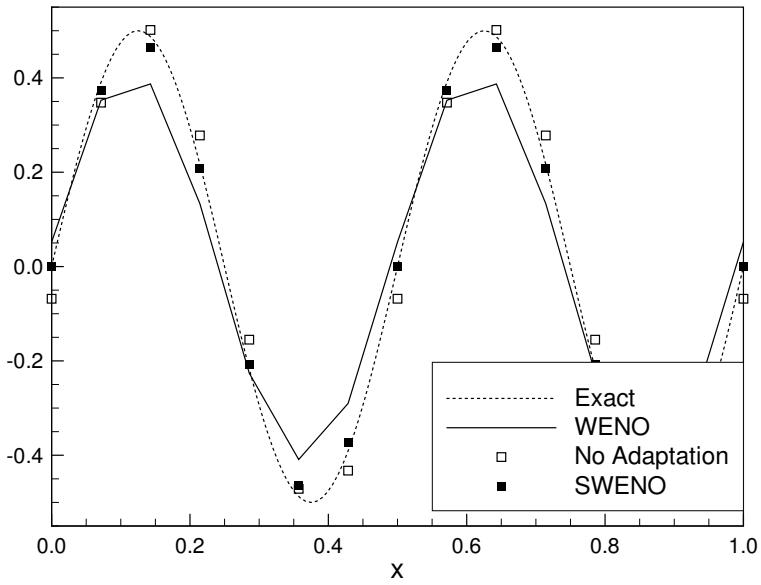

(a) Numerical and exact solutions.

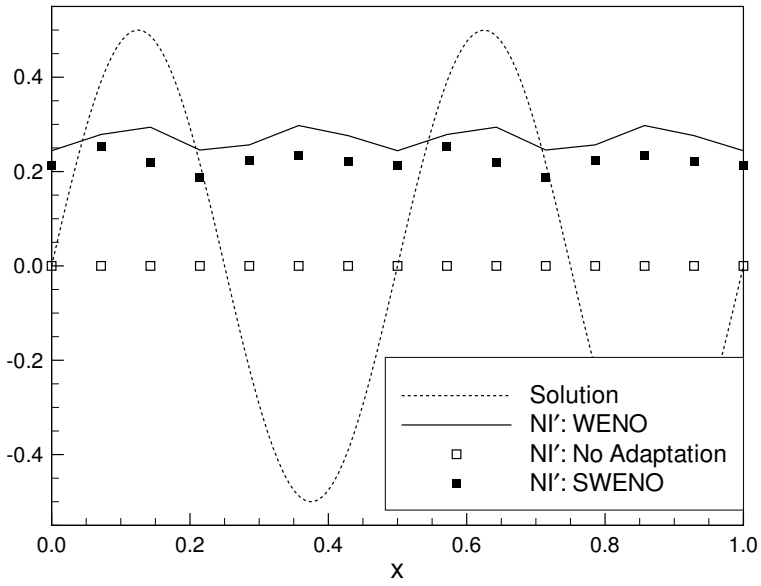

(b) Normalized nonlinearity index NI' layed over the exact solution.

Figure 2. Linearly advected sine wave with seven points per wavelength as computed by WENO-4 and synchronized WENO-4 (SWENO-4) schemes, with and without adaptation, after twenty wavelength-times.

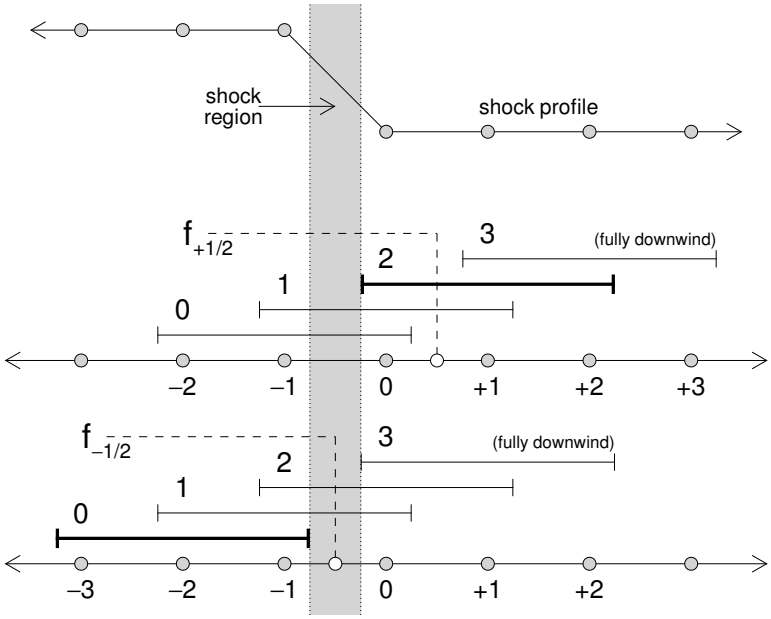

Figure 3. WENO-3 candidate stencils for approximating the numerical fluxes $\hat{f}^{+}_{i\pm 1/2}$ when a perfect shock is located somewhere between points x_{i-1} and x_i. Bold stencils are strongly weighted.

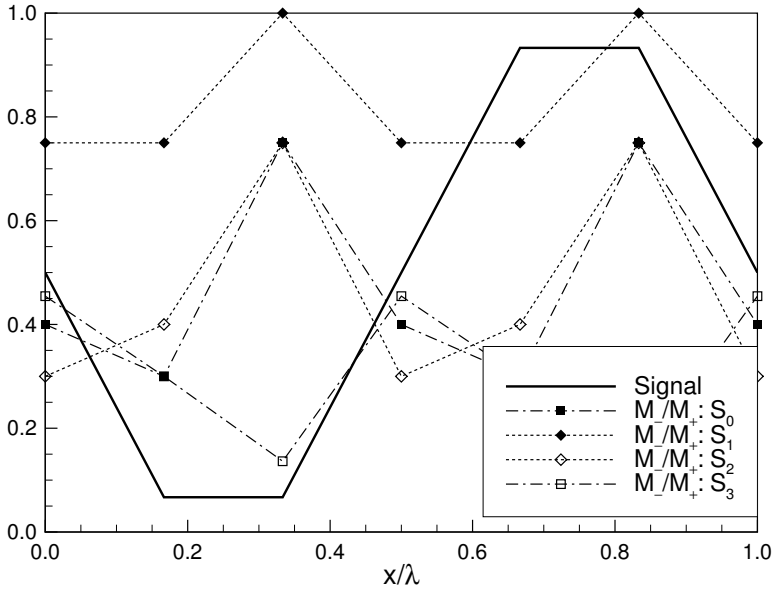

(a) WENO-3.

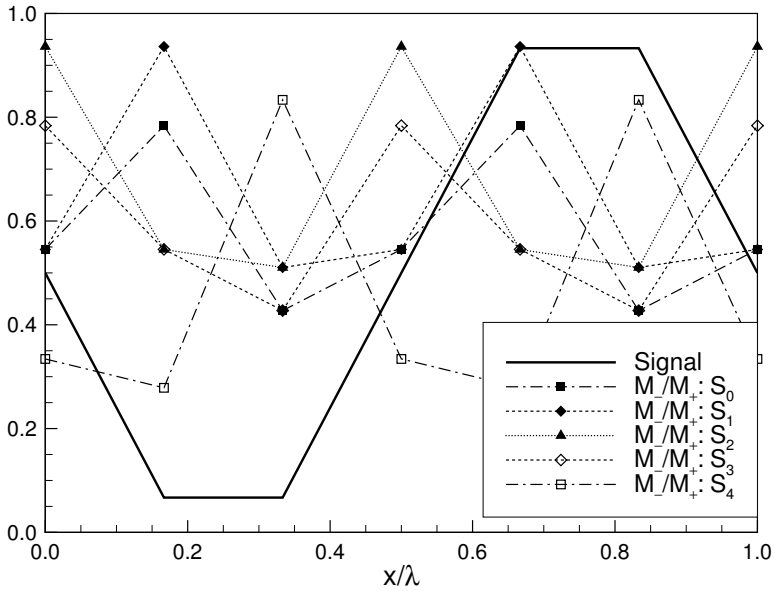

(b) WENO-4.

Figure 4. Left-versus-right weight ratio M_-/M_+ on each candidate stencil of the indicated WENO methods for an instantaneous sinusoidal signal with six points per wavelength.

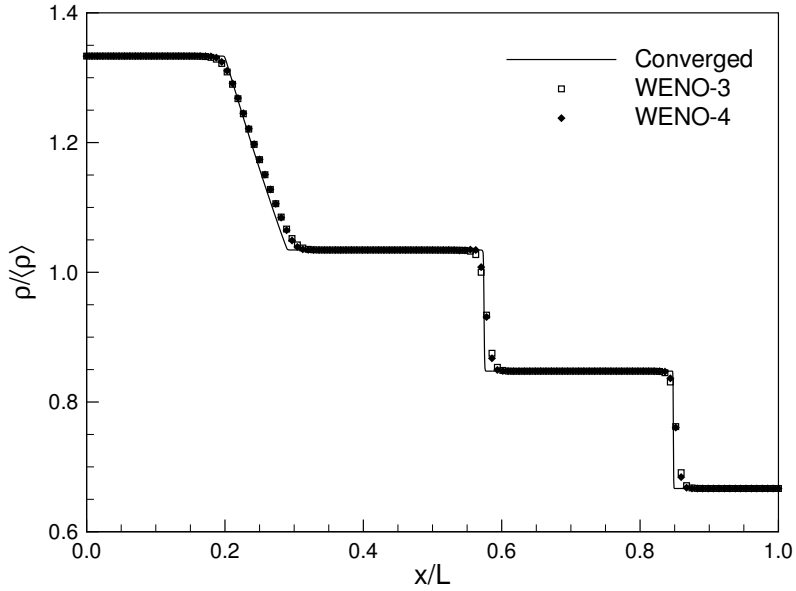

Figure 5. Density profile for the inviscid shock tube problem as computed by (unsynchronized) WENO-3 and WENO-4 schemes on 129 grid points.

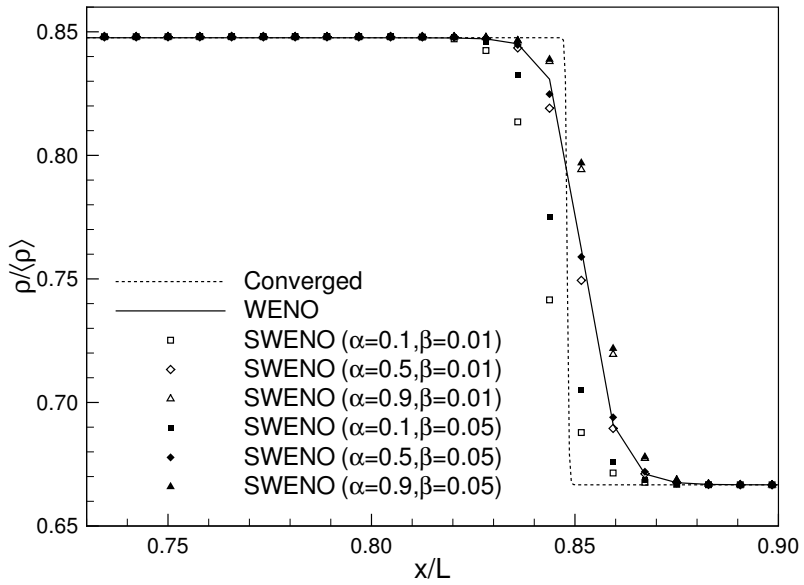

(a) Density profiles.

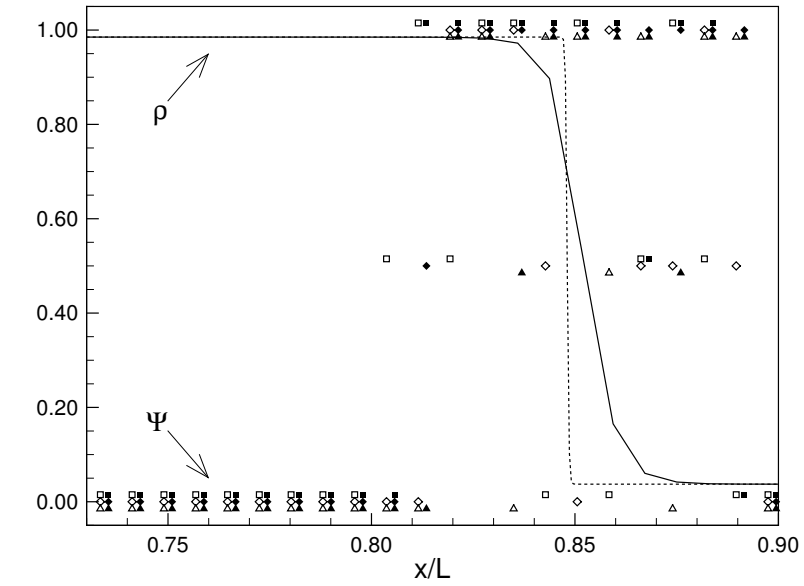

(b) Synchronization suspension indicator Ψ layed over a density profile sketch.

Figure 6. Shock from the shock tube solution of Fig. 5 as computed by WENO-3 and synchronized WENO-3 (SWENO-3) schemes with varying parameters α and β.

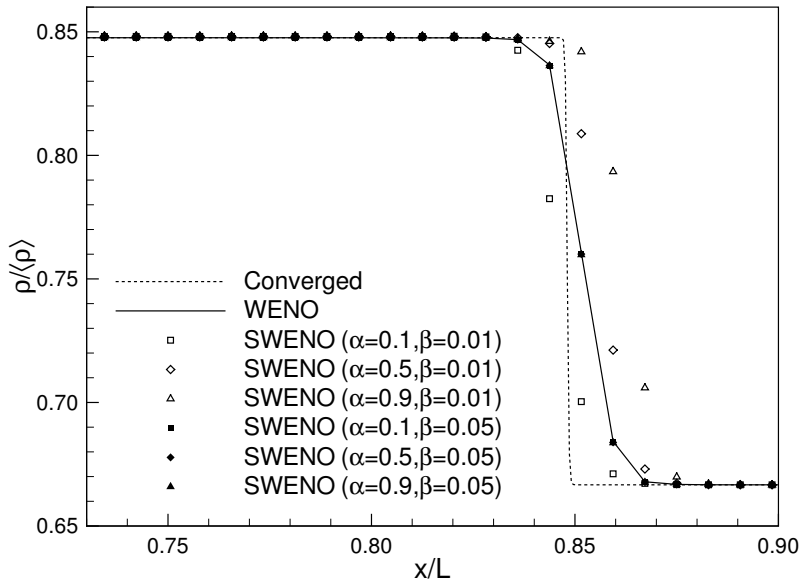

(a) Density profiles.

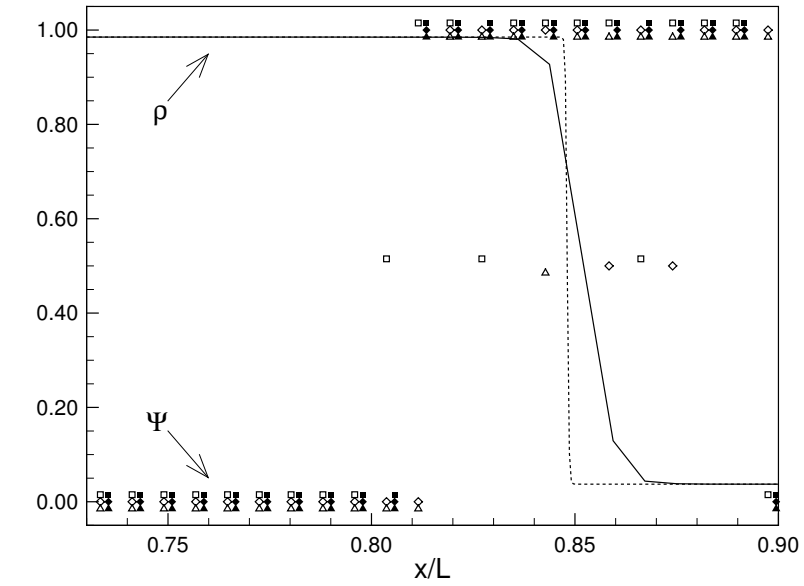

(b) Synchronization suspension indicator Ψ layed over a density profile sketch.

Figure 7. Shock from the shock tube solution of Fig. 5 as computed by WENO-4 and synchronized WENO-4 (SWENO-4) schemes with varying parameters α and β.

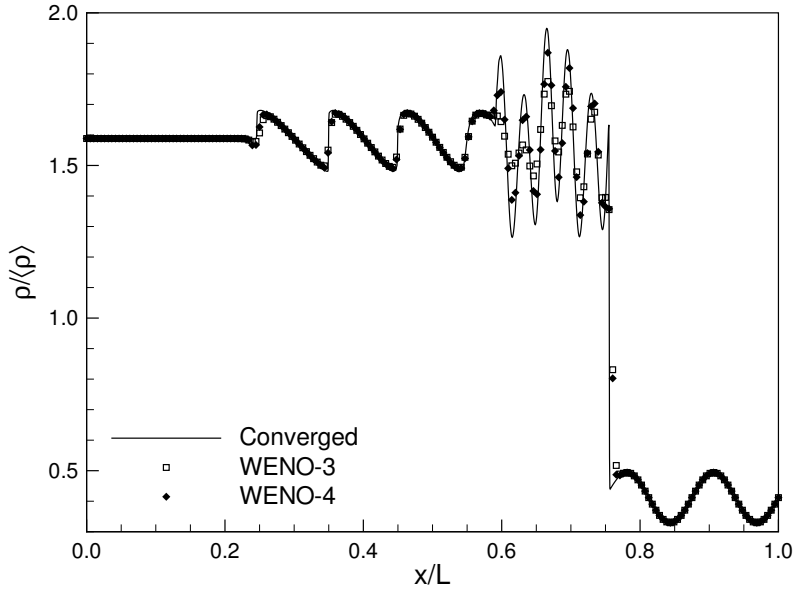

Figure 8. Density profile for the one-dimensional Shu-Osher problem as computed by (unsynchronized) WENO-3 and WENO-4 schemes on 193 grid points.

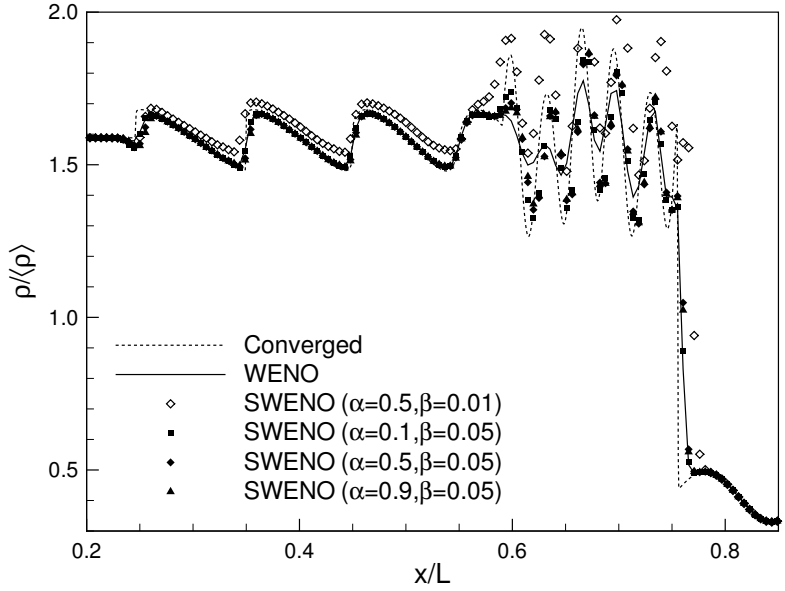

(a) Selected density profiles.

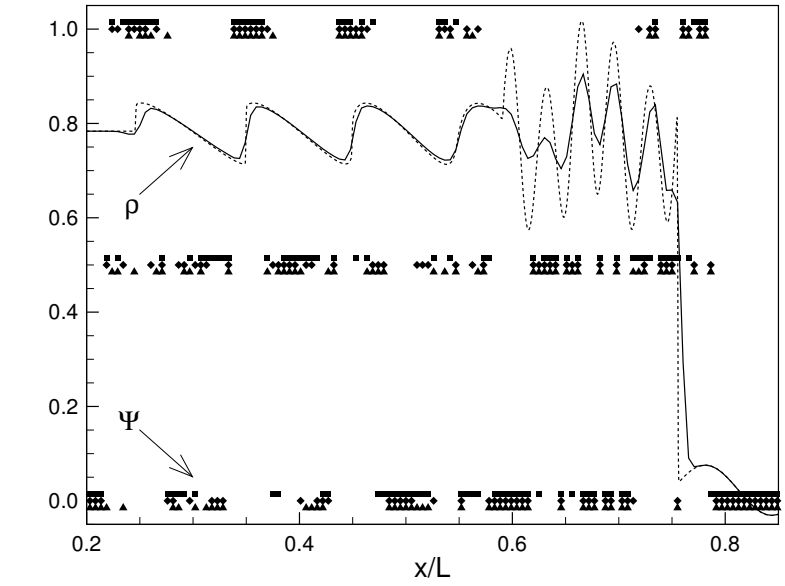

(b) Selected synchronization suspension indicators Ψ layed over a density profile sketch.

Figure 9. Fluctuations and main shock from the Shu-Osher problem of Fig. 8 as computed by WENO-3 and synchronized WENO-3 (SWENO-3) schemes with varying parameters α and β.

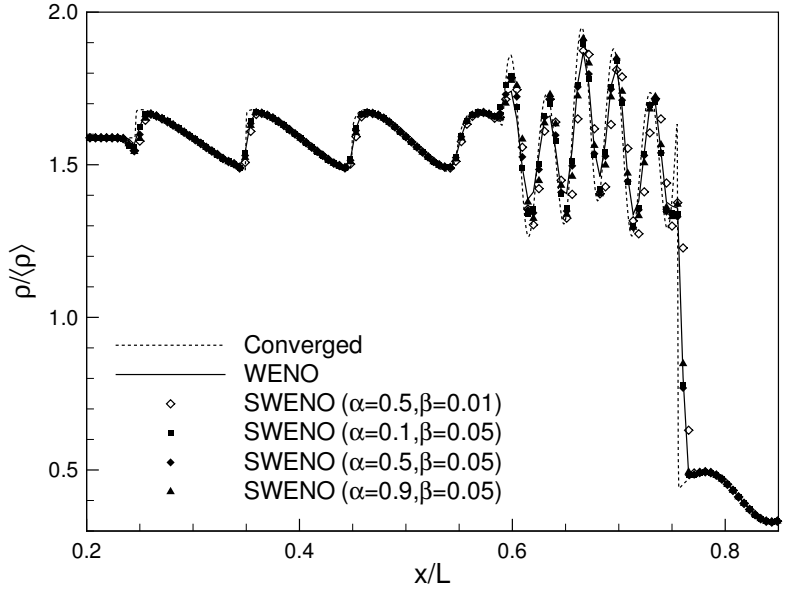

(a) Selected density profiles.

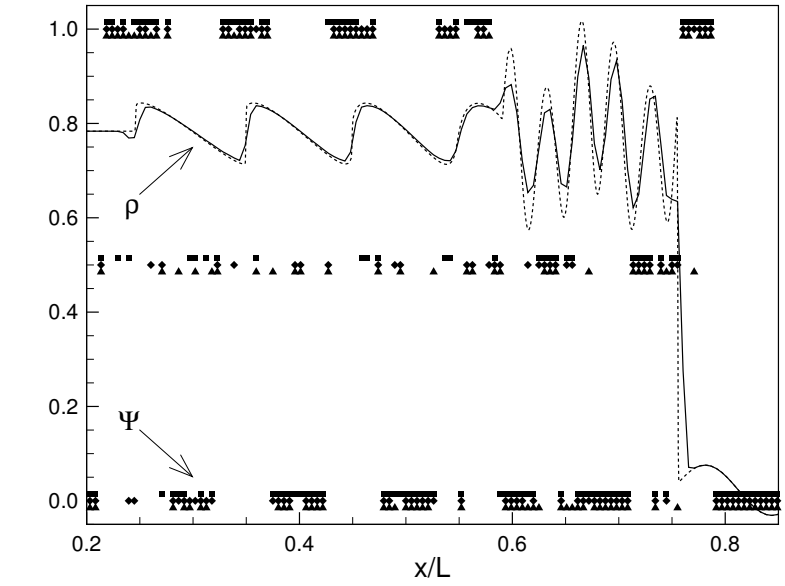

(b) Selected synchronization suspension indicators Ψ layed over a density profile sketch.

Figure 10. Fluctuations and main shock from the Shu-Osher problem of Fig. 8 as computed by WENO-4 and synchronized WENO-4 (SWENO-4) schemes with varying parameters α and β.

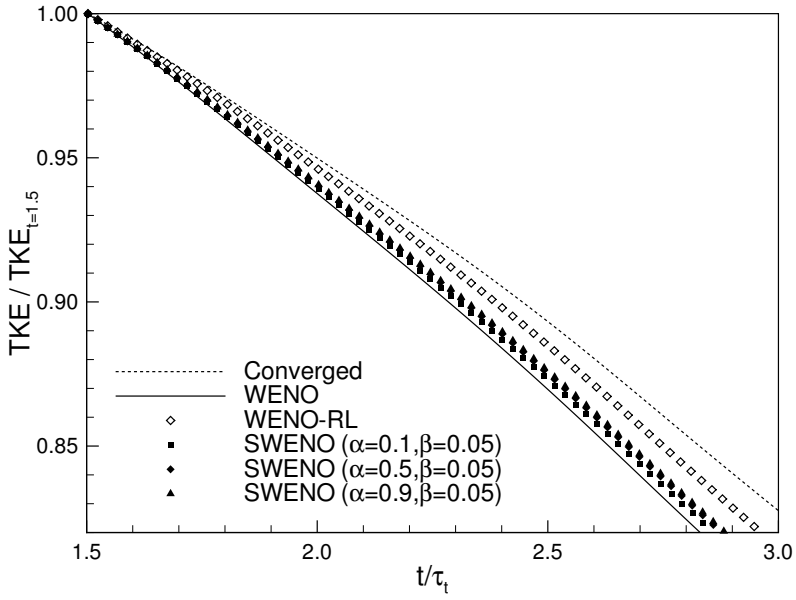

(a) Temporal evolution of average turbulent kinetic energy (normalized by its value at $t/\tau_t = 1.5$).

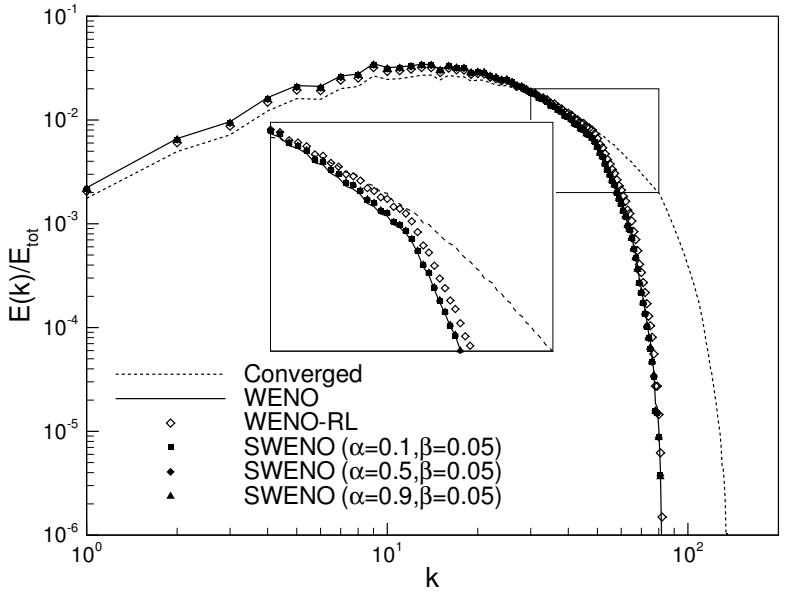

(b) Nondimensional energy spectrum at $t/\tau_t = 3.0$.

Figure 11. Compressible isotropic turbulence traits as computed by WENO-3, selected synchronized WENO-3 (SWENO-3), and, for comparison, relative-limited WENO-3 (WENO-RL-3) schemes on 96^3 grid points for initial $Re_\lambda = 50$ and $M_t = 0.7$.

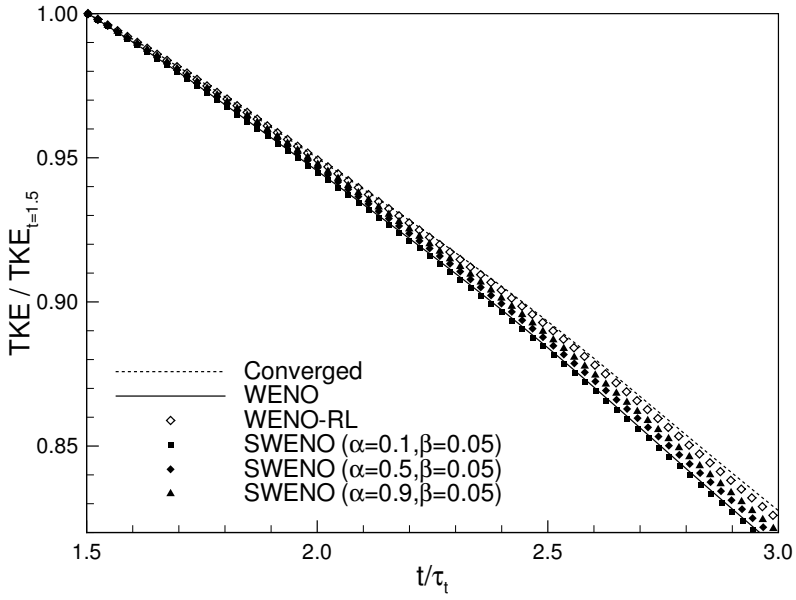

(a) Temporal evolution of average turbulent kinetic energy (normalized by its value at $t/\tau_t = 1.5$).

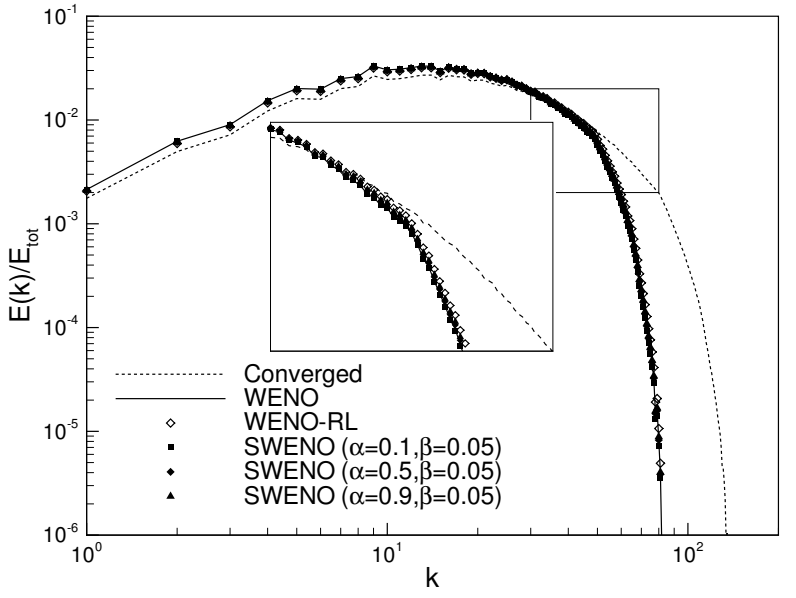

(b) Nondimensional energy spectrum at $t/\tau_t = 3.0$.

Figure 12. Compressible isotropic turbulence traits as computed by WENO-4, selected synchronized WENO-4 (SWENO-4), and, for comparison, relative-limited WENO-4 (WENO-RL-4) schemes on 96^3 grid points for initial $Re_\lambda = 50$ and $M_t = 0.7$.

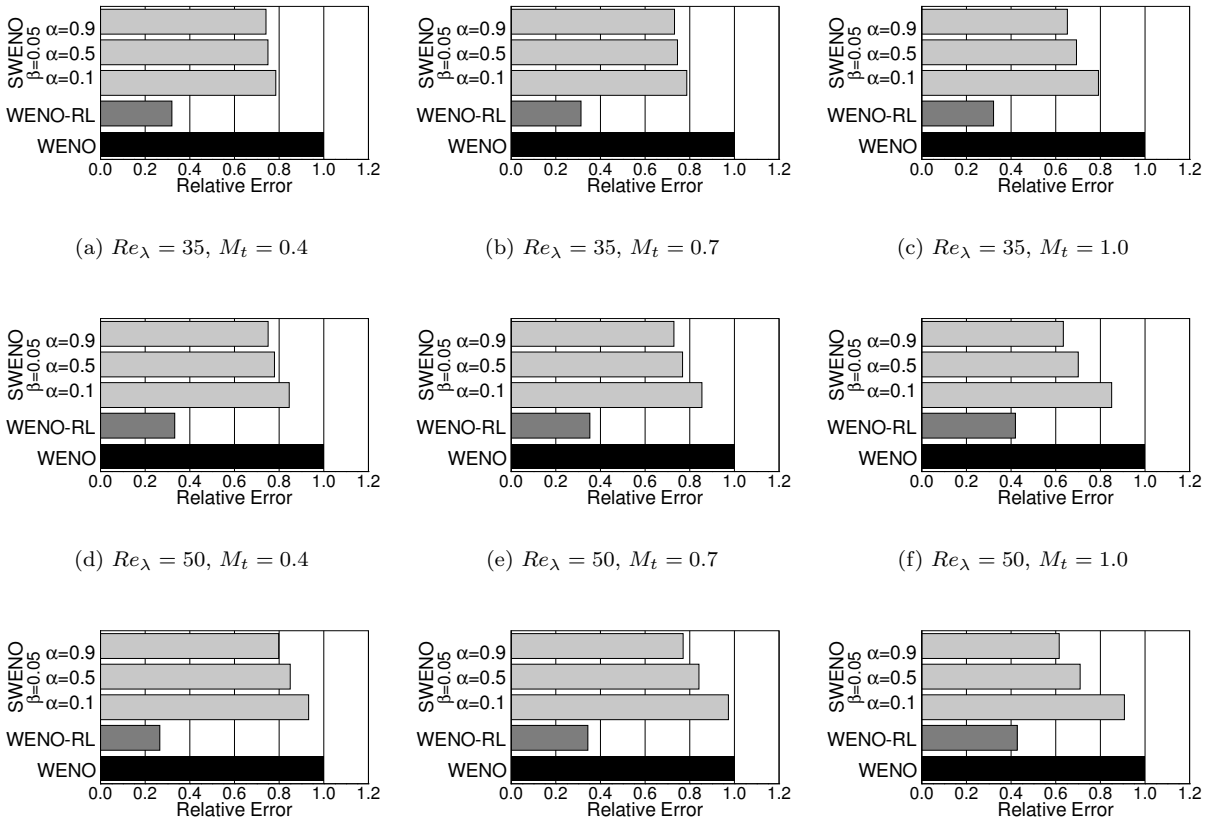

(a) $Re_\lambda = 35$, $M_t = 0.4$ (b) $Re_\lambda = 35$, $M_t = 0.7$ (c) $Re_\lambda = 35$, $M_t = 1.0$

(d) $Re_\lambda = 50$, $M_t = 0.4$ (e) $Re_\lambda = 50$, $M_t = 0.7$ (f) $Re_\lambda = 50$, $M_t = 1.0$

(g) $Re_\lambda = 75$, $M_t = 0.4$ (h) $Re_\lambda = 75$, $M_t = 0.7$ (i) $Re_\lambda = 75$, $M_t = 1.0$

Figure 13. Dissipative error in compressible isotropic turbulence produced by WENO-3, synchronized WENO-3 (SWENO-3), and, for comparison, relative-limited WENO-3 (WENO-RL-3) schemes for varying initial Re and M_t.

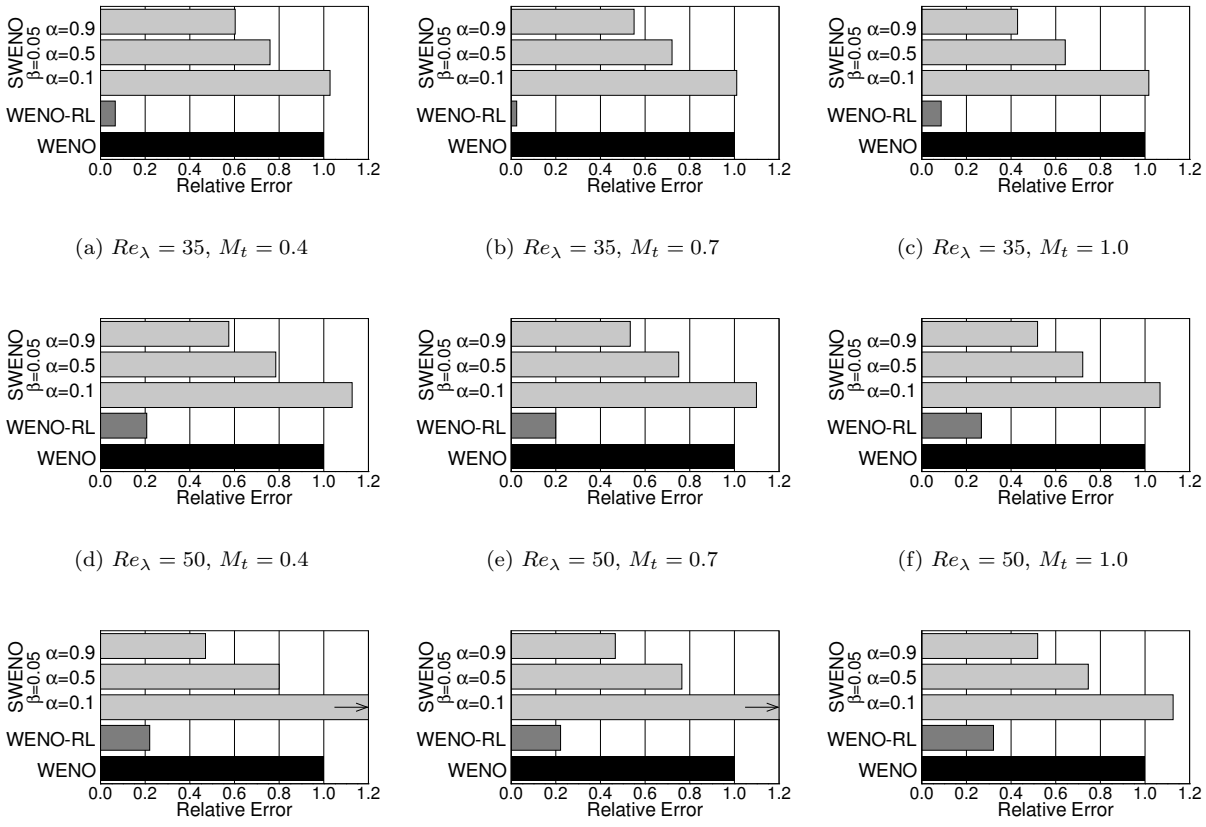

(a) $Re_\lambda = 35,\ M_t = 0.4$ (b) $Re_\lambda = 35,\ M_t = 0.7$ (c) $Re_\lambda = 35,\ M_t = 1.0$

(d) $Re_\lambda = 50,\ M_t = 0.4$ (e) $Re_\lambda = 50,\ M_t = 0.7$ (f) $Re_\lambda = 50,\ M_t = 1.0$

(g) $Re_\lambda = 75,\ M_t = 0.4$ (h) $Re_\lambda = 75,\ M_t = 0.7$ (i) $Re_\lambda = 75,\ M_t = 1.0$

Figure 14. Dissipative error in compressible isotropic turbulence produced by WENO-4, synchronized WENO-4 (SWENO-4), and, for comparison, relative-limited WENO-4 (WENO-RL-4) schemes for varying initial Re and M_t.